Sensors & Actuators: B. Chemical 326 (2021) 128956

Contents lists available at ScienceDirect

Sensors and Actuators: B. Chemical

journal homepage: www.elsevier.com/locate/snb

Hole-supply-rate-controlled methanol-gas-sensing reaction over *p*-type Co_3O_4/single-walled carbon nanotube hybrid structures

Nguyen Duc Chinh [a], Nguyen Manh Hung [a,b], Sutripto Majumder [a], Chunjoong Kim [a,*], Dojin Kim [a,*]

[a] Department of Materials Science and Engineering, Chungnam National University, Daejeon, 34134, Republic of Korea
[b] Department of Materials Science and Engineering, Le Quy Don Technical University, Hanoi, 100000 Viet Nam

ARTICLE INFO

Keywords:
Methanol sensing
Co_3O_4/SWCNT nanohybrid
p-p Heterojunction
Charge-controlled sensing

ABSTRACT

Co_3O_4/single-walled carbon nanotube (Co_3O_4/SWCNT) hybrid structures are fabricated, and their methanol sensing properties and related sensing principles are systematically investigated. A series of Co/SWCNT nanohybrid structures are deposited on silicon dioxide substrates by a co-arc discharge process and converted to Co_3O_4/SWCNT nanohybrid structures by subsequent methanol treatment and oxidation processes. The morphologies and structures of the nanohybrid composites are investigated by scanning electron microscopy, transmittance electron microscopy, X-ray diffraction, and Raman spectroscopy. The effect of the nanohybrid film thickness and the Co_3O_4: SWCNT ratio in the films on their physical and gas sensing properties are systematically examined. The best methanol-sensing performance is observed upon measurement at 300 °C for the material fabricated by deposition for 15 min and oxidized at 500 °C. The enhanced gas-sensing performance of the hybrid nanostructures is analyzed to prove that the high carrier supply rate from the transducer determines the reaction rate on the receptor surface (providing the receptor can accommodate the oxygen ionosorption). The hybrid sensor structures also exhibit low detection limit of 50 ppb, good selectivity, repeatability, and long-term stability, demonstrating their potential for practical application to methanol sensing.

1. Introduction

Detecting diseases through the volatile organic compound (VOC) signature of a patient's exhaled breath has long been recognized as having great potential as a rapid and noninvasive method for widespread screening and disease diagnosis [1,2]. Thus, the analysis of exhaled breath has been proposed as a convenient and safe diagnosis method complementary to blood and urine sampling [3,4]. Ongoing improvement of VOC analysis since the 1970s has allowed us to reconsider its role in medicine. The seminal 1971 paper by Linus Pauling presented a framework for the definition of human VOC profiles [5] and may be considered as a basis for the detection of anomalies that can be connected to specific pathologies.

Methanol is a VOC present in everyone's exhaled breath, and changes in the methanol concentration therein can be used to indicate lung cancer [6,7]. In developing countries, methanol poisoning outbreaks occur frequently with hundreds of victims due to adulterated alcohol as reported recently in Iran [8], Cambodia [9], and India [10]. The standard for detection of methanol intoxication is blood analysis by gas-liquid chromatography, which requires trained personnel while expensive and rarely available in developing countries. However, it was demonstrated that the methanol levels in blood can also be determined noninvasively in exhaled breath [11]. An ideal methanol sensor for breath testing should be sensitive to very low concentrations of methanol in the presence of environmental or physiological confounding factors. In addition, rapid and proportionate responses to small changes in concentration and consistent methanol-specific outputs are also required. Especially, it should possess good selectivity among VOCs (acetone and ethanol), hydrogen, carbon monoxide, nitrogen oxide, hydrogen sulfide, and less humidity dependence.

Nanomaterial-based sensing matrices have potential as clinical and laboratory diagnostic tools because they are smaller, easier to use, and less expensive than typical spectrometers and spectroscopes. Specifically, among the various metal-oxide semiconductors, *p*-type oxides may be suitable for the detection of VOCs based on their catalytic ability to promote the selective oxidation of VOCs [12]. In particular, typical

* Corresponding authors.
E-mail addresses: ckim0218@cnu.ac.kr (C. Kim), dojin@cnu.ac.kr (D. Kim).

https://doi.org/10.1016/j.snb.2020.128956
Received 7 April 2020; Received in revised form 16 September 2020; Accepted 22 September 2020
Available online 28 September 2020

p-type Co_3O_4 with a spinel structure is a strong candidate for such applications as it is a well-known high-density oxygen adsorbate having suitable catalytic activity and less sensitivity to humidity [13–15]. The pristine single-walled carbon nanotube (SWCNT) showed weak responses and low selectivity toward specific gas molecules due to the weak interaction between SWCNTs and analyte molecules, thus SWCNTs should be functionalized to enhance both the sensitivity and the selectivity [16–20]. The mixing of metal oxides with (SWCNTs) imparts various synergetic effects to the nanomaterial produced [21,22], and the hybridization of such oxides with SWCNTs can enhance their gas-sensing performances [23–26]. Furthermore, SWCNT sensors can work even at room temperature (RT) operation and allows easy miniaturization of the sensor structure for massive sensor arrays.

There have been very few reports about Co_3O_4/MWCNT composites as gas detecting sensors. Jung et al. [27] fabricated a Co_3O_4/MWCNT composite by electrodeposition for detection of hydrogen. We reported a Co_3O_4/MWCNT composite for detection of H_2S gas [25], but the gas selectivity investigation was limited to a few gases. In this extended study of Co_3O_4/MWCNT composite to more gas species, we found that the sensing performance to methanol is far better than to H_2S in the response level and response/recovery kinetics but at higher operation temperature. In addition to the examination of the methanol-sensing performance of the structure for the first time, we systematically controlled the Co_3O_4/SWCNT ratio in the composite to investigate the sensing mechanism in nanostructures of p-p heterojunction. Co_3O_4/SWCNT nanohybrid structures are directly deposited onto SiO_2 substrates by a co-arc discharge method we developed [25,26,28,29]. The film thickness and the ratio of Co_3O_4 nanoparticles to SWCNT bundles in the films were varied to find the sensor of optimum performance. Through the due procedure approaching the optimum structural condition of the sensor, the operating mechanism and principle of the composite sensors were discovered. We found that the hole-supplying rate from the SWCNT transducer to the Co_3O_4 receptor surface controls the rate of reaction between methanol and ionosorbed oxygen. We identified the origins of the enhanced sensing performances of the hybrid structure was the synergy effect of the high-conductivity SWCNTs acting as hole-supplying transducer and the Co_3O_4 nanoparticle receptor providing high oxygen adsorption sites. This interplay between the oxide receptor and carbon nanotube transducer seems to occur generally to all oxide-carbon nanotube composites establishing an optimum structural condition for sensing performance.

2. Experimental

2.1. Fabrication of Co_3O_4/SWCNT nanohybrid sensors

Co_3O_4 and SWCNT nanohybrid sensors were fabricated by a co-arc discharge method using SiO_2/Si substrates [25,26,28,29]. The substrate (5 mm × 5 mm × 0.65 mm, oxide thickness: 300 nm) was ultrasonically cleaned sequentially with acetone, methanol, and deionized water (15 min each), followed by blow-drying with nitrogen. Titanium (30 nm) and platinum (120 nm) were sequentially deposited onto the substrate using DC magnetron sputtering through a shadow mask patterned with two parallel electrode patterns. The electrode-patterned substrate was then mounted on the inside wall of the arc-discharge chamber as shown schematically in our previous report [29]. The active sensor area for Co_3O_4 and CNT deposition was defined by scotch-tape masking. The synthesis of the nanohybrid was carried out under the optimized conditions of an arcing current density of 40 A cm^{-2} in a hydrogen atmosphere with a partial pressure of 5.3×10^3 Pa, allowing the synthesized nanohybrid to attach directly to the substrate from the chamber interior. A pure graphite tube (length: 160 mm; outer diameter: 6.4 mm; and inner diameter: 3 mm) with cobalt wires inserted was used as the arc discharge source. The as-deposited film was dipped in methanol solution to enhance adhesion between the SiO_2 substrate and the Co_3O_4/SWCNT nanohybrid, providing good contact with the electrodes. The substrates were then dried on a hot plate at 100 °C for 15 min. In order to control the thickness of the nanohybrid films, the co-arc discharge deposition was performed for 2, 5, 10, 15, and 20 min, and all samples were heat-treated at 400 °C in air for 2 h to remove amorphous carbon residues and oxidize the cobalt metal to cobalt oxide [23]. These samples were labelled 2m-4, 5m-4, 10m-4, 15m-4, and 20m-4, respectively. A flowchart for the fabrication of the Co_3O_4/SWCNT nanohybrid sensors is shown in Fig. 1a. The oxidation temperature was also varied (500, 600, and 700 °C in air for 2 h) using 15-min deposited samples to control the SWCNT content of the nanohybrids by burning the SWCNTs out at different rates. This also changed the Co oxidation temperature. These samples were labelled 15m-5, 15m-6, and 15m-7, respectively. A pure SWCNT sensor was also fabricated using 15-min deposition and Co removal by etching in acid.

2.2. Structural characterization

The morphologies and crystal structures of the Co_3O_4/SWCNT nanohybrid structures were investigated by field-emission scanning electron microscopy (FE-SEM; JSM 700 F; JEOL, Japan), field-emission transmission electron microscopy (FE-TEM; Tecnai G^2 F30 S-TWIN, FEI, Netherlands), and X-ray diff ;raction (XRD; X'pert PRO-MPD, PANalytical, Netherlands). Their chemical structures were investigated by Raman spectroscopy (UniRAM spectrometer with an excitation line at 532 nm and a cooled charge coupled device detector).

2.3. Sensing property measurement

A schematic of the sensing measurement setup is shown in Fig. 1b. The nanohybrid sensor devices were mounted in a test chamber in which the sensor temperature and the gas flow rates can be precisely controlled by mass flow controllers (MFCs). The current at 1 V bias was measured as the gas-sensing signal using a picoammeter/voltage source (Keithley 6487). Saturated VOC vapors (methanol, ethanol, and acetone) were generated in a bubbler by blowing dry air through a pure VOC liquid solution. As the bubbler is a closed system comprising liquid and gas phases at thermal equilibrium we can apply the Antoine equation $Log(P_s)=a-b/(T+c)$, where P_s is the saturated vapor pressure, a, b, and c are the experimental constants for the given substance, and T is the temperature of the liquid-gas system [30]. The relative concentration of the substance in the gas phase (x_s) is calculated by $x_s=P_s/P$, where P is the

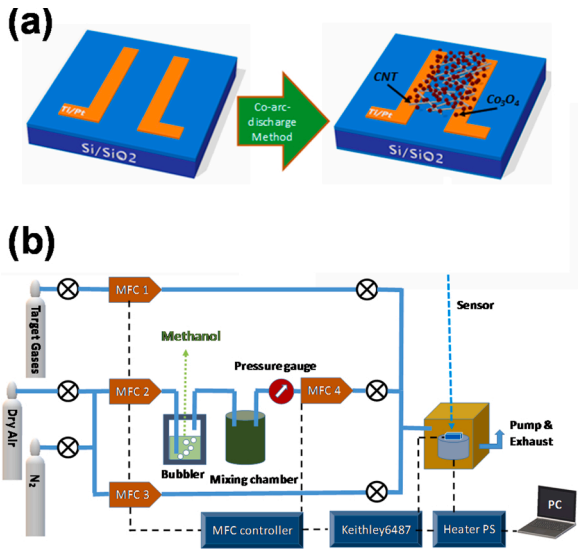

Fig. 1. (a) Flowchart for the fabrication of Co_3O_4/SWCNT nanohybrid sensors on SiO_2 substrates, and (b) the experimental set up for the gas-sensing property measurements under methanol flow.

total pressure of the system. The gas concentration, C, was determined using the relationship $C = C_{std} \times f / (f + F)$, where f and F are the flow rates of the analyte gas and carrier gas (dry air), respectively, and C_{std} is the analyte gas concentration in the cylinder or x_s for liquid sources. The response of the sensor, S, is defined by R_g/R_o for reducing gases (or R_o/R_g for oxidizing gases), where R_o is the standby resistance in dry air before exposure to the analyte gases and R_g is the resistance upon exposure to the analyte gases.

3. Results and discussion

3.1. Morphology and structure

Co-arc discharging of a cobalt-embedded graphite tube source evaporates the Co and graphite simultaneously to form Co nanomaterials with SWCNTs growing from the catalytic Co particles. The excess charging of Co into the graphite tube results in Co nanoparticles agglomerated with SWCNT bundles running through the particles. SEM images of the fabricated Co_3O_4/SWCNT nanohybrid structures after oxidation at 400 °C for various deposition times (from 2 to 20 min) are shown in Fig. S1 and Fig. 2a. The images clearly evidence the similar morphologies of the agglomerated porous Co_3O_4 nanoparticles. The thickness of the films monotonically increased from 100 to 450 nm with increasing deposition time from 2 to 20 min, as shown in the figure inserts. Although the SWCNT bundles synthesized are barely observed by SEM, they run through the Co_3O_4 nanoparticles forming Co_3O_4/SWCNT nanohybrid composites. The Co_3O_4 nanoparticles vary in size from several to tens of nanometers and their sizes do not vary with synthesis time.

Fig. 2a–d shows SEM images of Co_3O_4/SWCNT nanohybrids deposited for 15 min, followed by oxidation at 400, 500, 600, or 700 °C. They reveal that oxidation temperature has no effect on Co_3O_4 particle size (although very slight grain growth is observed for oxidation at 700 °C). It has been previously demonstrated that SWCNTs burn away in the temperature range 400–600 °C [31,32]. Therefore, 15m-7 may contain only Co_3O_4 nanoparticles and a negligible amount of CNTs. The TEM image shown in Fig. 2e reveals a morphology of the composite showing entangled Co_3O_4 particles with SWCNT bundles. The high-resolution TEM image of Fig. 2f reveals the SWCNT bundles comprising Co_3O_4 nanoparticles. The inset reveals typical lattice fringe of spinel cubic Co_3O_4 by the spacing of 0.24 nm corresponding to the (311) planes, which was also supported by XRD analysis (see below).

The XRD patterns of the Co_3O_4/SWCNT nanohybrid structures oxidized at different temperatures are shown in Fig. 3a. The peaks at 26.5° and 43° correspond to the (002) and (100) lattice planes of the SWCNTs, respectively (JCPDS, #75-1621) while the peaks at 19°, 31.3°, 36.8°, 39.3°, 44.9°, 56.5°, 59.5°, and 65.3° correspond to the (111), (220), (311), (222), (400), (422), (511), and (440) lattice planes of the spinel cubic Co_3O_4 (JCPDS, #00-042-1467). Only peaks for the spinel cubic Co_3O_4 phase are shown for the samples oxidized at 400–700 °C and no impurity peaks are presented. Diffraction peaks for the SWCNTs are visible for samples oxidized at temperatures up to 600 °C but not at 700 °C, indicating that the 15m-7 sample comprises only Co_3O_4 nanoparticles due to burning out of the SWCNTs.

The Raman spectra shown in Fig. 3b confirm the XRD results. All the samples show five typical peaks at 188, 474, 517, 609, and 680 cm^{-1}, which are ascribed to the F_{2g}, E_g, F_{2g}, F_{2g}, and A_{1g} Raman-active modes, respectively, of Co_3O_4 [33]. The normal spinel structure of crystalline Co_3O_4 is in the form $Co^{2+}(Co^{3+})_2\ O_4^{2-}$, where Co^{2+} and Co^{3+} are placed at tetrahedral and octahedral sites, respectively [34]. Also shown are the Raman spectra for SWCNTs, which typically consist of two major peaks at ~1340 cm^{-1} and ~1600 cm^{-1}, which are termed the D-band and G-band, respectively [35]. The D-band is induced by sp^3 electronic states and is associated with defective/disordered graphite and glassy carbon, while the G-band is related to the sp^2 vibration of the two-dimensional hexagonal lattice in the graphite. The very high G-band peak intensity compared with that of the D-band is a typical feature of highly crystalline SWCNTs [36]. The G-band to D-band peak intensity ratios (I_G/I_D) of the SWCNTs are ~4 for 15m-4 and ~4.5 for 15m-5, indicating the high quality of the as-synthesized SWCNTs. Furthermore, the decreasing intensity of the G-band peaks with increasing oxidation temperature clearly indicates burn-away of the CNTs in the hybrid structures. No D- and G-band peaks are observed for 15m-7, indicating that the SWCNTs are completely burnt away leaving behind only Co_3O_4 nanoparticles. As such, the SWCNTs to Co_3O_4 volume ratio in the nanohybrid structures is controlled by the oxidation temperature.

3.2. Electrical properties

The current-voltage (I–V) characteristics of the Co_3O_4/ SWCNT nanohybrid sensor films with different thicknesses (2m-4, 5m-4, 10m-4, 15m-4, and 20m-4) were measured in the range -2–2 V at room temperature (~25 °C) in dry air, as shown in Fig. S2. Prior to measurement, the films were heated to 350 °C in dry air to desorb water molecules from the surface and then allowed to cool to room temperature. All the hybrid structures exhibit good ohmic contact, as shown by the perfectly linear I–V curves. The current increases with increasing deposition time from 2 to 20 min and with increasing film thickness.

The I–V measurements at varying temperatures (from 200 to 350 °C) for the thickness-varied series of sensor structures oxidized at 400 °C generated the conductance (G) data via the relationship $I = GV$, as summarized in Fig. 4a. The conductance of the Co_3O_4/SWCNT nanohybrid structures increases with temperature, demonstrating the semiconducting nature of the structures. The conductance increases with film thickness as the cross-section area of the conduction channel increases due to the geometry of the sensors, as shown in Fig. 1a. The linearity of the conductance in the Arrhenius form $[G \propto \exp(-\Delta E/k_B T)]$ indicates thermal activation of the conduction. The calculated activation energies (ΔE) for conduction are 0.56, 0.51, 0.45, 0.39, and 0.37 eV for 2m-4, 5m-4, 10m-4, 15m-4, and 20m-4, respectively. These energies are also depicted in Fig. 4c. The continuous decrease in activation energy with increasing film thickness could be partially due to the higher degree of percolation among the high-conductance SWCNTs as the films become thicker and partially due to the delayed SWCNT synthesis in the initial arc-discharging stage, which is illustrated in Fig. S3.

The effect of Co_3O_4:SWCNT ratio on the conductance of the nanohybrid sensors was also investigated by the temperature-dependent conductance measurements, as summarized in Fig. 4b, in which those of pure SWCNTs and pure Co_3O_4 (i.e., sample 15m-7) are included for comparison. As discussed above, the different Co_3O_4:SWCNT ratios in the samples were realized by employing different oxidation temperatures. Clearly shown is the highest conductance of the SWCNT, leading to the lowest activation energy for conductance (~0.06 eV) among the structures. The mixing of Co_3O_4 particles into the SWCNT network reduces the conductance by several orders of magnitude in the order 15m-4 > 15m-5 > 15m-6 > 15m-7 as the SWCNT content decreases (Fig. 4b). Furthermore, the temperature dependence of G, or dG/dT, becomes steeper with increasing Co_3O_4 content in the hybrids. The activation energies measured are 0.39, 0.64, 0.74, and 0.97 eV, respectively, as is also plotted in Fig. 4c. It is shown that the Co_3O_4:SWCNT ratio has a much larger effect on conductance than film thickness. The higher oxidation temperature of the hybrids enhances the crystallinity of the Co_3O_4 nanoparticles, thereby reducing the hole concentration therein [37]. The conductance of the SWCNTs is approximately six orders of magnitude higher than that of the pure Co_3O_4 at 300 °C (Fig. 4b). All these observations indicate that the high-conductivity SWCNTs act as conduction channels in the nanohybrid structures of 15m-4 to 15m-6. Therefore, the conduction of the hybrid structures can be modeled by a parallel circuit comprising two resistors; high-resistance Co_3O_4 and low-resistance SWCNTs. In the parallel circuit, the conductances of the hybrid structures are mainly determined by the SWCNT content of the

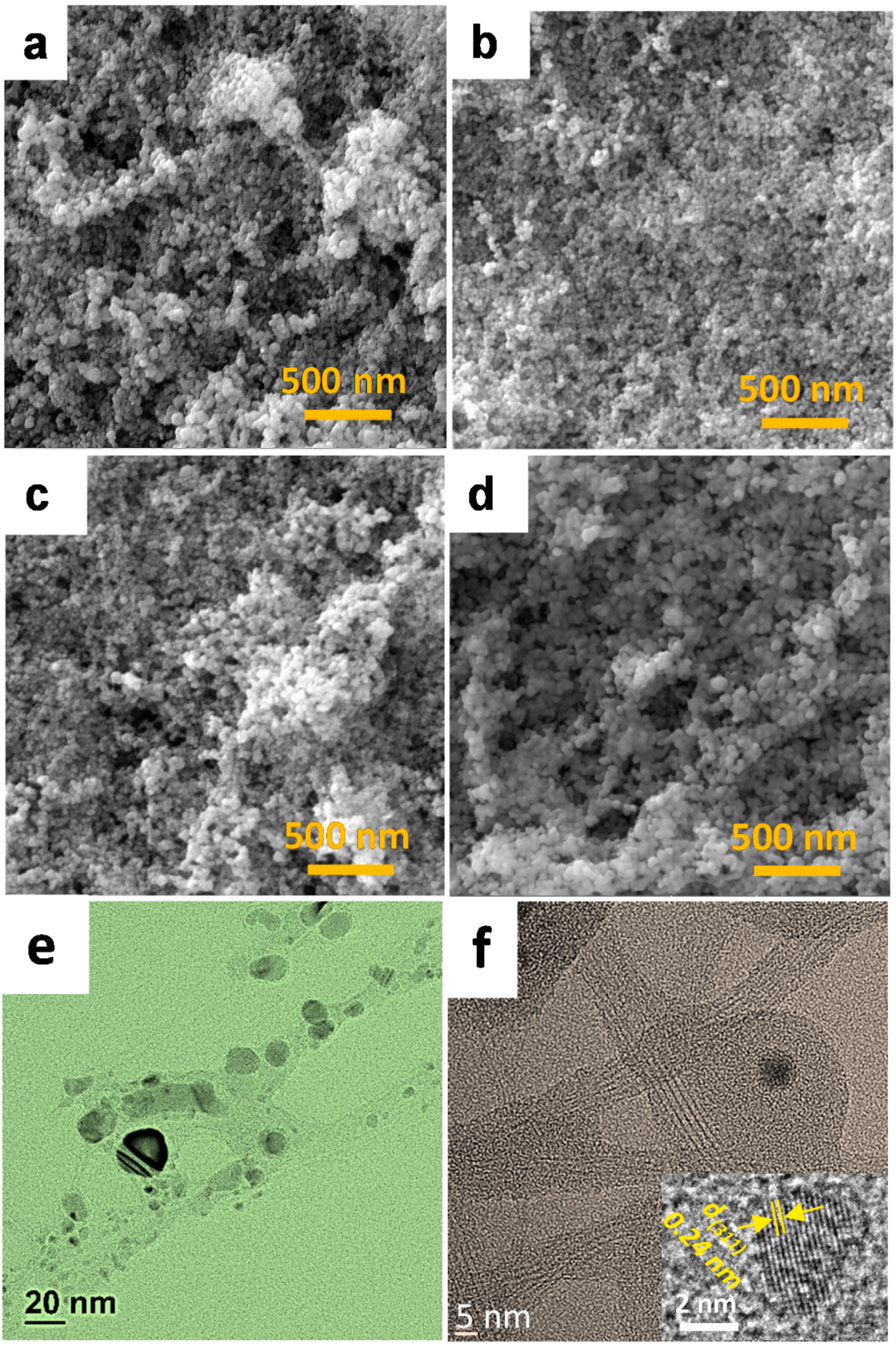

Fig. 2. SEM images of Co_3O_4/SWCNT nanohybrids deposited for 15 min followed by oxidation at various temperatures: (a) 400 °C, (b) 500 °C, (c) 600 °C, and (d) 700 °C. (e, f) TEM images of 15m-5 with different magnifications showing SWCNT bundles containing Co_3O_4 particles. The lattice fringes for Co_3O_4 is shown by the insert.

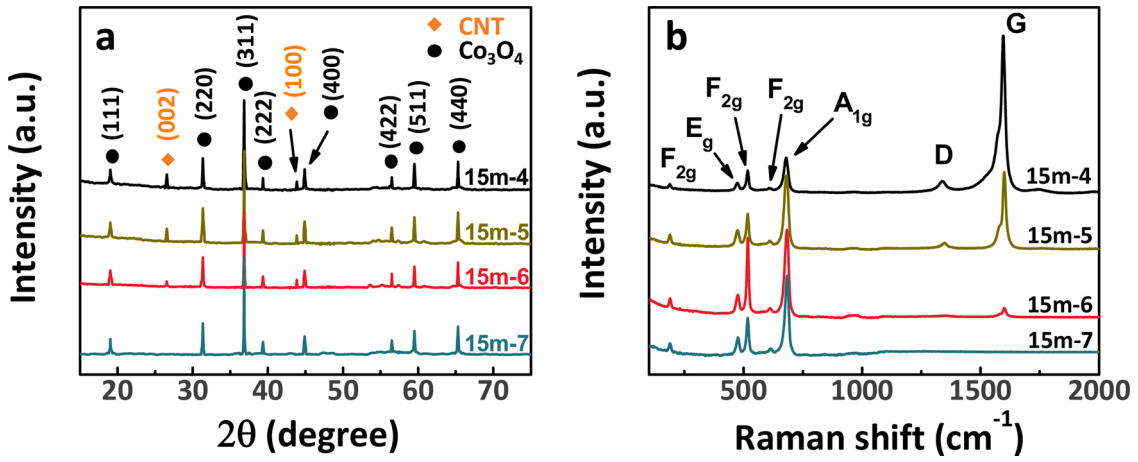

Fig. 3. (a) XRD patterns and (b) Raman spectra of the Co_3O_4/SWCNT nanohybrid structures oxidized at 400, 500, 600, and 700 °C.

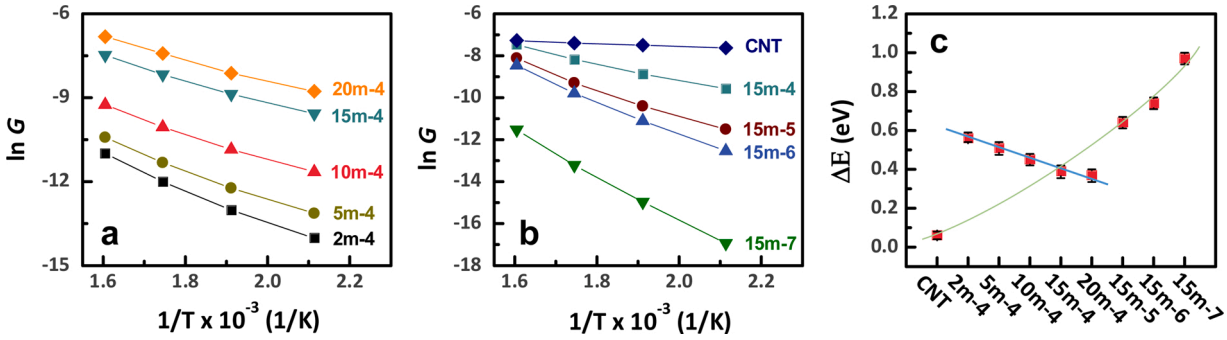

Fig. 4. Conductance vs. temperature for different (a) hybrid film thicknesses and (b) Co_3O_4:SWCNT ratios. (c) Activation energies obtained from (a) and (b).

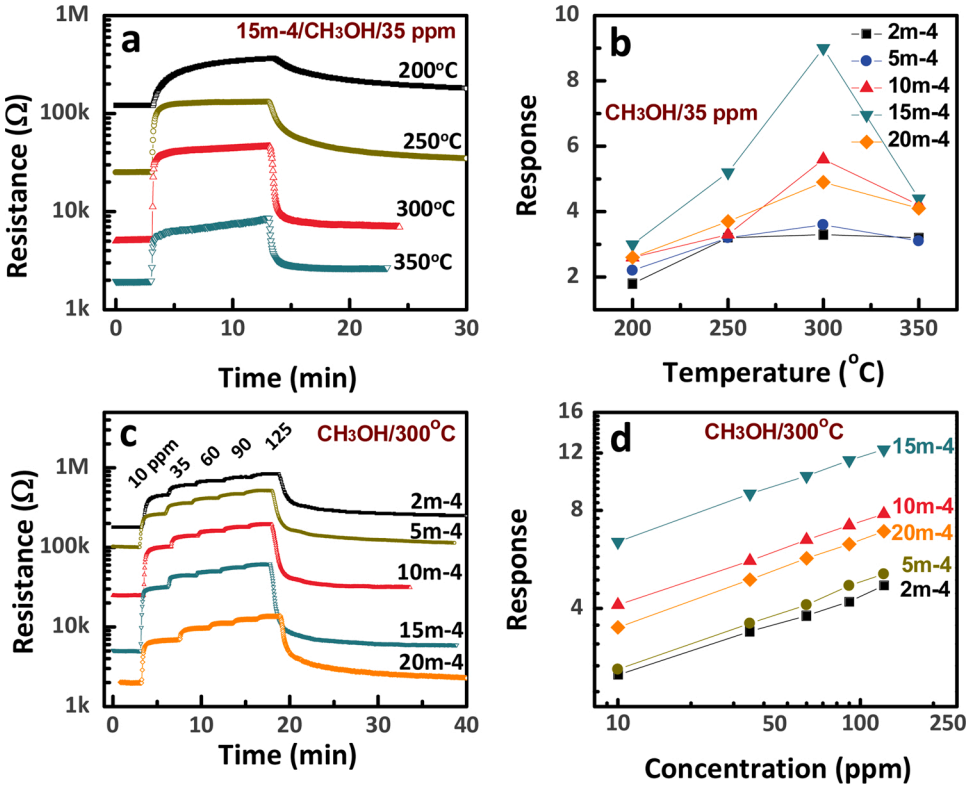

Fig. 5. (a) Response-recovery curves for the 15m-4 sensor to 35 ppm methanol gas measured at different working temperatures from 200 to 350 °C. (b) Response levels to 35 ppm methanol of the nanohybrid sensors as a function of working temperature, demonstrating that the highest response occurs at 300 °C. (c) Transient responses of the sensors as a function of methanol concentration (10–125 ppm) measured at 300 °C. The results are summarized in (d), showing the linearity of the response to methanol concentration.

structures owing to their intrinsically high hole concentration.

3.3. Sensing properties

The response-recovery behaviors to 35 ppm methanol gas of the Co_3O_4/SWCNT nanohybrid sensor structures having different film thicknesses (2m-4, 5m-4, 10m-4, 15m-4, and 20m-4 sensors) were evaluated at various working temperatures from 200 to 350 °C. The results for the 15m-4 sensor are shown in Fig. 5a and those of the others in Fig. S4a–d. Increasing of resistance upon exposure to reducing gases signifies a *p*-type semiconducting behavior. All the sensors show *p*-type sensing behavior because both Co_3O_4 and SWCNT are *p*-type semiconducting materials. The temperature dependence of the response level measured for the sensors is summarized in Fig. 5b, which shows the highest response level at 300 °C for all the Co_3O_4/SWCNT nanohybrid sensors with different film thicknesses. The sensor responses are rapid and saturate within 10 min at >250 °C. The 15m-4 sensor with a thickness of 350 nm exhibits the maximum response level (S ~9) at 300 °C. Fig. 5c shows the transient responses to methanol gas concentrations of 10, 35, 60, 90, and 125 ppm measured at 300 °C, where the gas concentration was changed at 3 min intervals. The results are summarized in Fig. 5d, which shows that the response level increases linearly with gas concentration in the range 10–125 ppm. The hybrid sensors of different film thicknesses exhibit largely linear concentration dependence, although their response levels are different. Thus, the results confirm that the hybrid structures are potential methanol sensors.

The response signals originate from the chemical reaction between the impinging methanol molecules and the adsorbed oxygen ions on the surface of the sensor materials, the SWCNTs, and/or Co_3O_4 nanoparticles. The reaction forms volatile CO_2 and H_2O gases leaving empty adsorption sites (S_A) behind on the surface, and the reaction generates electrons that transfer into the sensor body, as in Eq. 1.

$$CH_3OH + 3O^-_{ad} \rightarrow CO_2 + 2H_2O + 3e^- + 3S_A \quad (1)$$

The emptied oxygen ionosorption sites are then occupied by impinging oxygen molecules from the environment while acquiring electrons from the sensor body through Eq. 2.

$$O_2 + 2e^- + 2S_A \leftrightarrow 2O^-_{ad} \quad (2)$$

The interplay of the two molecular dynamic processes continues during the response cycle finally reaching the response level. At the saturated response level, the reaction rate of Eq. 1 is equal to the rate of oxygen ionosorption in Eq. 2 onto the surface. The response rate measures how quickly the steady state is reached. In the recovery cycle, the reaction in Eq. 2 continues reversibly when the reaction in Eq. 1 has stopped. The process again reaches the steady state, where the adsorption and desorption rates for oxygen molecules on the receptor surface are equal.

The transient response-recovery properties of 15-min deposited sensors having different Co_3O_4:SWCNT ratios were investigated. The response-recovery curves to 35 ppm methanol gas measured at different working temperatures from 200 to 350 °C are displayed in Fig. S5a-d for 15m-5, 15m-6, 15m-7, and pure SWCNTs, respectively. The sensing response levels for the Co_3O_4/SWCNT hybrids with different Co_3O_4:SWCNT ratios are compared in Fig. 6a, including those for pure Co_3O_4 (15m-7) and pure SWCNTs. The response-recovery time is defined as the time taken to reach 90 % of the final steady state resistance value (T90 %), and the results are summarized in Fig. 6b and c.

Fig. 6a show that the pristine SWCNT sensor exhibits negligible response (~1.1) over the entire temperature range examined (200 – 350 °C). This is not because of the lower reaction rate of Eq. 1 caused by a low oxygen ionosorption density on the SWCNT surface, but rather because of its very high conductance, which leads to a small overall conduction change, as will be shown. In contrast, the response of pure Co_3O_4 (15m-7) is higher than that of the SWCNTs, exhibiting the highest level of ~5 at 350 °C. Compared with these two structures, the nanohybrid sensors 15m-4, 15m-5, and 15m-6 exhibit much higher response levels at the optimum operation temperature of 300 °C. Among the hybrid structures, the 15m-5 sensor exhibits the highest response level of ~21, which is approximately 5.5- and 19.5-times greater than those of the pure Co_3O_4 and SWCNT sensors, respectively. The optimum operation temperature of 300 °C for the hybrids, which is lower than that of the pure Co_3O_4 (Fig. 6a) were benefited by the SWCNT [21,22]. Therefore, the mixing of SWCNTs with Co_3O_4 nanoparticles produces synergetic improvements in the response level and working temperature for methanol detection.

The clear trends observed in Fig. 6b and c are that the response and recovery kinetics are enhanced at i) higher temperatures and ii) higher SWCNT contents. The temperature dependence of the response and recovery rates is understandable because both the rate of reaction between the ionosorbed oxygen species and the methanol molecules as well as the oxygen adsorption/desorption rate are accelerated as the temperature increases. It should be noted, however, that the response and recovery times monotonically decrease with SWCNT content in the structures, suggesting the important kinetic role of the SWCNTs. The response and recovery times for the optimal structure (15m-5) are 150 and 180 s, respectively, at 300 °C.

The response levels and sensing kinetics are clearly related to the material hybridization. Thus, we further analyzed the results to demonstrate the advantages of the hybrid nanostructures. Fig. 7a shows the response-recovery curves to 35 ppm methanol gas measured at 300 °C by sensors with different Co_3O_4:SWCNT ratios. The methanol sensing signal is defined by the ratio of the resistances before and after the surface reaction with methanol molecules (R_o and R_g, respectively), i.e., $S = R_g/R_o$. Fig. 7b summarizes the raw data in terms of R_o, R_g, and $\Delta R = R_g - R_o$ values as read from Fig. 7a. The data can be also presented by $S = I_o/I_g$, where I_g and I_o are the current in the presence and absence of the analyte gas, respectively. This conversion is useful because the

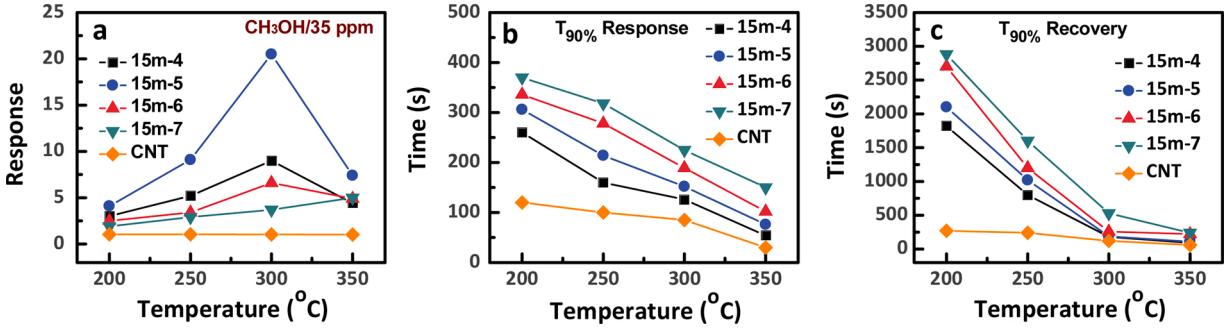

Fig. 6. (a) Response levels to 35 ppm methanol for nanohybrid sensors with different Co_3O_4:SWCNT ratios (15m-4, 15m-5, and 15m-6) measured as a function of working temperature. The data from the pure Co_3O_4 (15m-7) and the pristine SWCNT sensors are compared. (b) Response and (c) recovery times (T90 %) to 35 ppm methanol measured at different working temperatures.

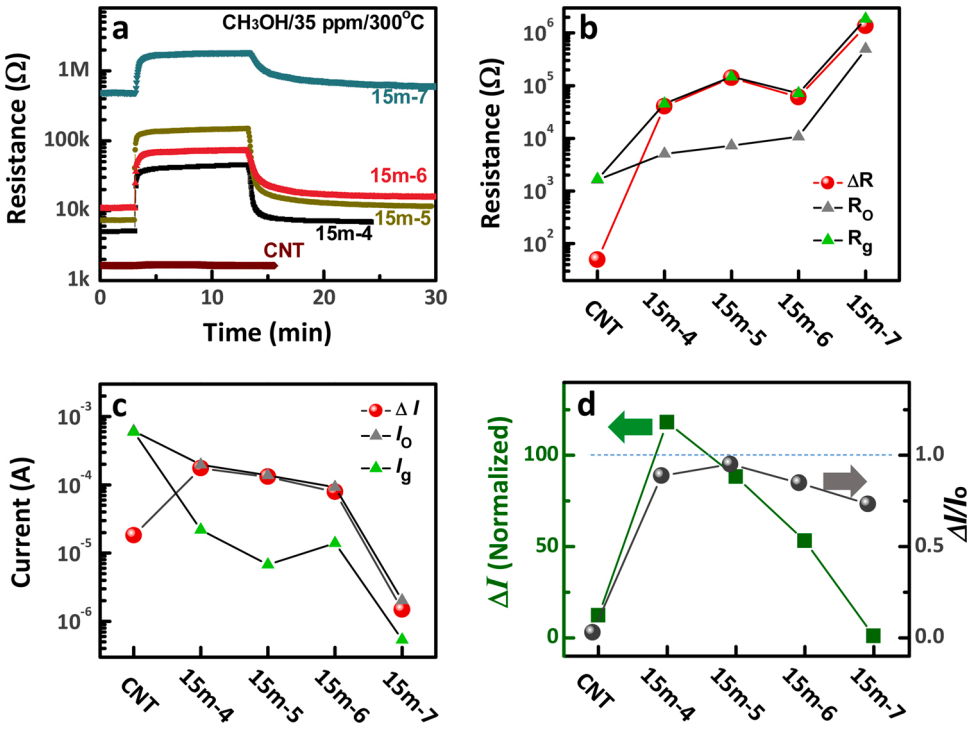

Fig. 7. (a) Transient response curves to 35 ppm methanol at gas 300 °C for the SWCNTs and hybrid sensors. (b) R_o, R_g, and ΔR values extracted from (a). (c) I_o, I_g, and ΔI values converted from (b). (d) ΔI values normalized with respect to that of pure Co_3O_4. Also shown is $\Delta I/I_o$ as a measure of the decrease in the abundance of hole carriers in the structure due to the methanol reaction on the surface.

current is the flow rate of the charges derived from the surface gas reactions. Fig. 7b is replotted in Fig. 7c using the corresponding current data I_o, I_g, and $\Delta I = I_o - I_g$ measured at 1 V. The current changes for different hybrid structures are presented in Fig. 7d in two different forms, i.e., ΔI, which is the absolute charges transferred for the response but normalized to that of pure Co_3O_4, and $\Delta I/I_o$, which shows the charge ratio for the response.

The results can be summarized as follows:

i) As the Co_3O_4:SWCNT ratio increases, the current (I_o) monotonically decreases from $\sim 6 \times 10^{-4}$ A for the SWCNTs to $\sim 2 \times 10^{-6}$ A for pure Co_3O_4. I_o is $\sim 10^{-4}$ A for the hybrids.

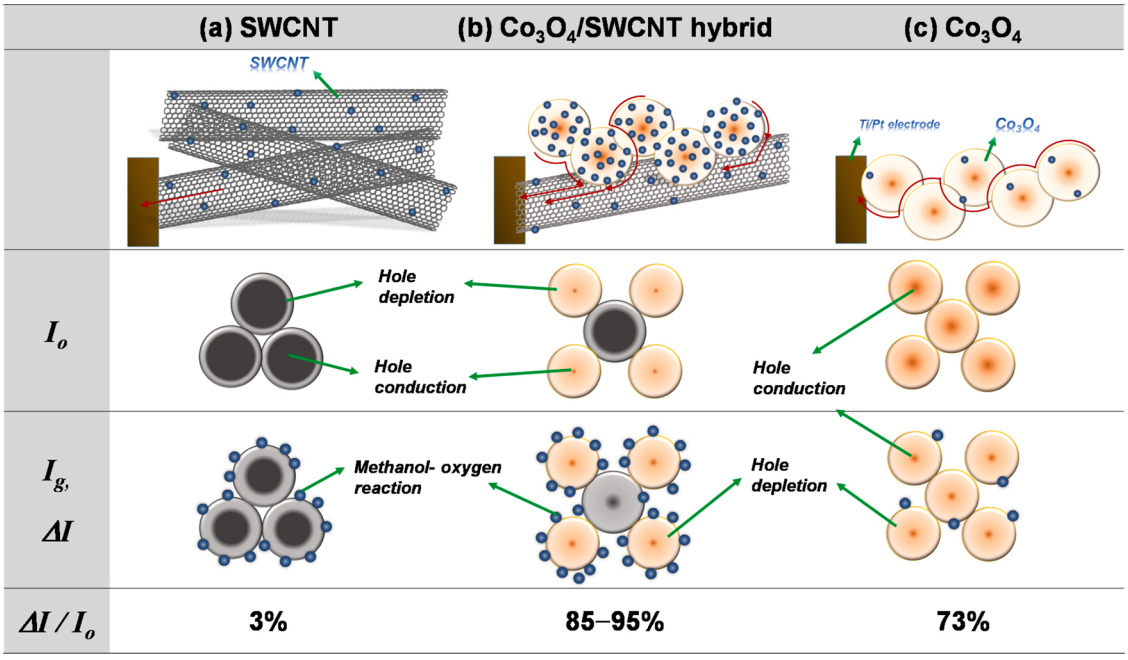

Fig. 8. Schematics of the sensor conditions for (a) SWCNTs, (b) Co_3O_4/SWCNT hybrids, and (c) Co_3O_4. A comparison of the morphologies and cross-sections showing the change in the conduction and depletion areas before (I_o) and after (I_g) the methanol reaction is also given. The frequency of the methanol reaction at the surface (ΔI) is shown by blue dots on the surface. The travel distance for the electrons is different, as denoted by the red arrows, due to the different sensor morphologies (For interpretation of the references to colour in this figure legend, the reader is referred to the web version of this article).

Because I_o for the SWCNTs is ~300-times greater than that for Co_3O_4, I_o for the hybrids is mainly dictated by the conduction through the SWCNTs in the structures.

ii) The change in current (ΔI) upon reaction with methanol are $\sim 2 \times 10^{-5}$ A for the SWCNTs, $\sim 10^{-4}$ A for the hybrids, and $\sim 2 \times 10^{-6}$ A for Co_3O_4 (Fig. 7c). This highlights two remarkable aspects of this work. The first is that ΔI for the SWCNTs is higher than that for the Co_3O_4. The absolute value ΔI (the number of methanol molecules reacted on the surface) for the SWCNTs is ~12-times higher than that for the Co_3O_4. The second is the synergetic effect exhibited by the hybrids. The ΔI values for the hybrids are $50-120$-times that of the Co_3O_4 and $4-12$-times that of the SWCNTs, as summarized in Fig. 7d.

iii) The $\Delta I/I_o$ ratio is much lower for the SWCNTs than for the other samples. As methanol impinges into the structure, only 3% of the holes in the SWCNT are supplied for the methanol reaction on the surface, while 89 %, 95 %, 85 %, and 73 % of the holes in the structures are supplied in 15m-4, 15m-5, 15m-6, and 15m-7, respectively (Fig. 7d).

3.4. Nanosensor mechanism and principles

As discussed earlier, the conduction in the hybrid structures may be modelled by a parallel conduction circuit comprising the SWCNTs and Co_3O_4 particles. The current in the hybrids may then be represented by Eq. 3.

$$I_o = I_{o,\mathrm{SWCNT}} + I_{o,\mathrm{Co}} = (A_{\mathrm{SWCNT}}\sigma_{\mathrm{SWCNT}} + A_{\mathrm{Co}}\sigma_{\mathrm{Co}})F \quad (3)$$

Here, A_{SWCNT} is the cross-sectional area of the SWCNT bundles and A_{Co} is that of the Co_3O_4 nanoparticle network. σ_{SWCNT} is the conductivity of the SWCNTs and σ_{Co} is that of the Co_3O_4. F is the electric field. We observed that $A_{\mathrm{SWCNT}}\sigma_{\mathrm{SWCNT}} \approx 300 \cdot A_{\mathrm{Co}}\sigma_{\mathrm{Co}}$ in Fig. 7c, and the SWCNTs are barely observed in SEM pictures (thus, $A_{\mathrm{SWCNT}} \ll A_{\mathrm{Co}}$ in Fig. 2). Thus, $\sigma_{\mathrm{SWCNT}} \gg \sigma_{\mathrm{Co}}$. The literature values previously reported are $\sigma_{SWCNT} = 10^4 - 10^6$ S/cm [38] and $\sigma_{Co} = 10^{-7} - 10^{-3}$ S/cm [37,39] at room temperature. The I_o values decrease in the order I_o(SWCNT) >> I_o(hybrids) >> $I_o(Co_3O_4)$. Therefore, the monotonically decreasing I_o as oxidation temperature increases (Fig. 7c) results from the decreasing A_{SWCNT} term under the relatively small $A_{\mathrm{Co}}\sigma_{\mathrm{Co}}$ term. The different cross-sectional areas of the conduction channels in the center of the materials are depicted schematically in Fig. 8. The largest conduction channel area for the SWCNTs and the smallest for the Co_3O_4 are illustrated for I_o, while the intermediate cross-section areas for the hybrids are shown for the SWCNTs in contact with Co_3O_4.

The observation given for ii) above is that ΔI(hybrids) >> ΔI(SWCNT) >> $\Delta I(Co_3O_4)$. ΔI represents the total flux of the methanol molecules reacting with the ionosorbed oxygen molecules on the receptor surface as represented by different numbers of blue dots for ΔI in Fig. 8. If the current from the reaction in Eq. 1 is denoted by $I_{(1)}$ and from the reaction of Eq. 2 by $I_{(2)}$, ΔI can be presented by $\Delta I = I_{(1)} - I_{(2)}$. Then, a higher ΔI requires a higher $I_{(1)}$ or a higher reaction rate for Eq. 1, while $I_{(2)}$ is not independently controlled [29,40,41]. Firstly, the result ΔI(hybrids) >> I(SWCNT) indicates that the increased $I_{(1)}$ in the hybrids is acquired mostly from the enhancement due to the Co_3O_4, not directly from the SWCNTs, because the SWCNT content is lower in the hybrids. Secondly, the result ΔI(hybrids) >> $\Delta I(Co_3O_4)$ indicates that the increased $I_{(1)}$ for the hybrids is also driven by the SWCNTs in the hybrids because the reaction rate on the Co_3O_4 surface without the SWCNTs is very low, as indicated by the small value of $\Delta I(Co_3O_4)$. We postulate that, in the hybrids, the Co_3O_4 nanoparticles provide the receptor surface for oxygen ionosorption and the SWCNTs act as transducers that supply holes to the Co_3O_4. Such separate roles for SWCNTs and attached oxides in composites has been observed frequently in the literature [26].

The response signal level, however, is not determined by ΔI but by the ratio $I_o/I_g \approx \Delta I/I_g$. In relation to the response level, we measured the ratio $\Delta I/I_o$, which we call the 'charge transfer ratio', and this is the number of holes depleted by the methanol reaction over the number of holes contained in the sensor before the reaction. The measured values of $\Delta I/I_o$ are 3%, 85–95 %, and 73 % for the SWCNTs, hybrids, and Co_3O_4, respectively, and these different depletion region depths in I_g are also depicted in Fig. 8. The first remarkable observation is the very low $\Delta I/I_o$ ratio (and thus the small response level) for the SWCNTs compared to that of the Co_3O_4 although ΔI is significantly higher for the SWCNTs. The very small depletion region compared to the large cross-section shown with I_g in Fig. 8a explains the occurrence in the SWCNT. The SWCNTs as highly conductive hole reservoirs behave like a thick bulk sensor, where the condition $d \cdot N_A >> n_s$ applies (d is the dimension of the sensor unit, N_A the hole concentration in the sensor, and n_s the surface adsorption-site-density for oxygen) [26,29]. The other extreme case is illustrated by the Co_3O_4 sensor (Fig. 8c), which is a network of nanoparticles whose sizes are at the scale of the depletion depth, as shown with I_o in Fig. 8c. The condition $d \cdot N_A \sim n_s$ applies, and only a few holes can be supplied to the surface reaction toward the total depletion of holes in the Co_3O_4 particles, leading to a small ΔI, as illustrated with I_g in Fig. 8c. However, I_o is also small and $\Delta I/I_o$ can have a high value as observed.

Based on the results above, we further discuss the synergy effect revealed in the Co_3O_4/SWCNT hybrid structures for methanol sensing here. The higher oxidation temperature improves the crystallinity of the Co_3O_4 [37], which may reduce the density of oxygen adsorption sites on the surface. However, we approximate that the volume and size of the Co_3O_4 nanoparticles are not very different through the hybrid structures. Under this assumption, what we observed in the hybrids are i) high ΔI values, and ii) ΔI data overlapping on the I_o data (or high $\Delta I/I_o$ ratios), as shown in Fig. 7**c**. Actually, the order(s)-of-magnitude-higher ΔI for the hybrids are driven by the high hole supply rate from the SWCNTs until the almost complete depletion of holes from the SWCNT transducer, as indicated by the high $\Delta I/I_o$ values of 85–95 % and represented by the almost depleted SWCNT for I_g in Fig. 8b. Therefore, we see that the holes are freely supplied to the Co_3O_4 receptors from the SWCNTs, leading to an enhanced $I_{(1)}$. Because almost all the holes are exhausted from the SWCNTs ($\Delta I \approx I_o$), we assert that the methanol reaction on the Co_3O_4 receptors is fast and the hole-supply rate determines the gas sensing kinetics and thus determines $I_{(1)}$. Ultimately, the hole-supply rate controls the synergetic sensing process in the hybrid structures.

The synergetic effect supplied by the hybridization also improves the sensing response-recovery kinetics, as observed in Fig. 6**c** and d. The effect originates from the mixing with SWCNTs, and the response-recovery time decreases with increasing SWCNT content. Therefore, the enhancement of sensing rate is due to the increased rate of hole supply from the SWCNTs to the receptor surface. This indicates that the SWCNTs offer a fluent electrical pathway for rapid migration of electrons and holes, which dictates the sensor performance of the composite structure. The activation energy for conduction that decreases with increasing SWCNT content (Fig. 4b and c) explains the fact that the hole-supply rate varies with increasing SWCNT content.

The electron/hole transport kinetics as well as the synergy effect observed are considered in terms of carrier transport in energy band diagrams. In order to draw heterojunction band bending at the interface, information on the electron affinity (E_A), bandgap energy (E_g), and doping for each material are necessary. Several studies have concluded that the E_A (~4.5 eV) and E_g for SWCNTs vary with chirality, length, diameter, and doping [42–44] so that a mixture of various kinds of SWCNTs can behave like metals. The optically measured values for Co_3O_4 are $E_A = 3.65$ eV and $E_g = 2.1$ eV [45], but the data for E_g scatter in the range 1.6–2.8 eV [46,47]. Furthermore, the properties of the materials we fabricated can be different, and therefore a conclusive drawing of band alignment interfaces is difficult. However, despite these uncertainties, we can assume that the conduction band offset at the SWCNT/Co_3O_4 interface will be large while the valence band offset is

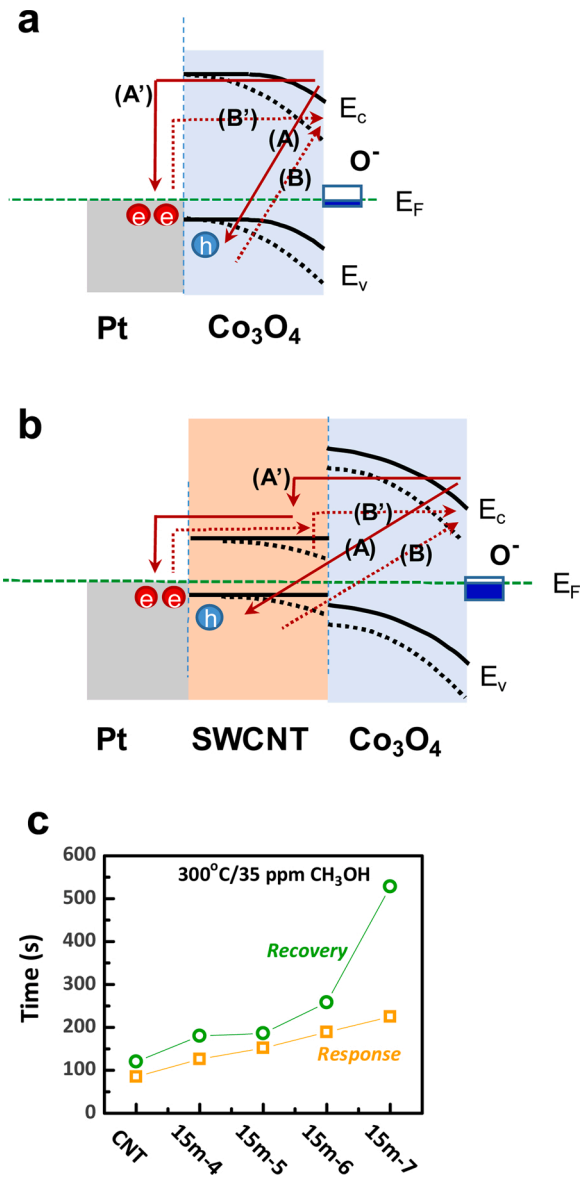

Fig. 9. Energy band diagrams for (a) Pt/Co_3O_4 and (b) Pt/SWCNT/Co_3O_4 hybrids at thermal equilibrium. The processes (A) and (A') with the solid band diagram represent the electron movement in the response cycle for the methanol reaction, and the processes (B) and (B') with the dotted band diagram show the electron movement in the recovery cycle for oxygen adsorption. (c) Response and recovery times to 35 ppm methanol at 300 °C for the hybrid structures taken from Fig. 6c and d. It shows a sudden increase of the recovery time in pure Co_3O_4.

smaller because both Co_3O_4 and SWCNTs are *p*-type doped materials. Therefore, the Pt electrode/SWCNT metallic contact will have negligible resistance to carriers, but the Pt/Co_3O_4 interface will have a large conduction band offset.

The electron and hole products of the surface reactions transport to the Pt electrode as a current signal. The band diagram for the 15m-7 sensor, which is composed of a Co_3O_4 nanoparticle network, can be sketched as shown in Fig. 9a. Note that the band bends down at the *p*-Co_3O_4 surface, which is depicted following the Mott-Schottky measurement results [48,49]. Since oxygen ionosorption with electron capture causes an upwards band bending, the Mott-Schottky measurement results indicate that processes other than oxygen ionosorption occur at the surface, causing the downward bending at the Co_3O_4 surface. Also, if the oxygen ionosorption energy level (which is depicted as aligned at the Fermi level (E_F) in Fig. 9) of a material is not a function of doping, a downward band bending should be observed for *p*-type doping.

The sensing signal of the Co_3O_4 sensor is determined by the current flow along the series of Co_3O_4 nanoparticles. In the response cycle of the methanol reaction in Eq. 1, the electrons are released at the Co_3O_4 surface. The band diagram of the initial status of oxygen ionosorption is presented by solid line, and that under the methanol flux by a dotted line in Fig. 9a. In the response cycle, the electrons released recombine with the holes in the Co_3O_4 nanoparticles (process (A)) or travel to the Pt electrode via the surface route at lower conduction band energy (process (A')). However, the recombination process (A) is limited due to the limited number of holes available in the nano-sized particles, and the probability of the long migration passing through many particles will be low, as illustrated in Fig. 8c. Therefore, although 73 % of the holes in the Co_3O_4 nanoparticles are depleted in the response cycle, the total amount of depleted holes is small, as evidenced by the low ΔI value. Conversely, the reverse processes are required in the recovery cycle. Electrons have to be supplied either by the electron-hole pair generation process (B) or by transfer from Pt along the particle surfaces (process (B') in Fig. 9a). Both processes have low probability due to the high energy barrier involved. The sudden increase in recovery time for the Co_3O_4 sensor (15m-7) shown in Fig. 9**c** reflects the high energy barrier in the recovery cycle.

Compared to the Co_3O_4 sensor performance, the synergy effect observed with the hybrid structures is explained using the energy band diagram of the Pt/Co_3O_4/SWCNT heterojunction shown in Fig. 9b. The most dramatic difference from the Co_3O_4 sensor in terms of morphology is that the Co_3O_4 particles are closely connected to nearby SWCNTs. In the response cycle, the released electrons can recombine freely with the holes in neighboring SWCNTs without traveling long distances (Fig. 8b, and process (A) and (A') in Fig. 9b). The orders-of-magnitude-larger number of holes in the SWCNTs support a high rate of oxygen release (ΔI). It should be noted that the high ΔI is possible because of the high density of ionosorbed oxygen on the Co_3O_4 surface under the high hole-density supply from the SWCNTs. The ionosorbed oxygen density is much higher for the hybrids than for the pure Co_3O_4, which is depicted by the highly filled up O^- states at the surface in Fig. 9b. In the recovery cycle, the electron transport rate to the Co_3O_4 surface can be enhanced through the cascading conduction bands via the SWCNT step-stone, as illustrated by the process (B') in Fig. 9b. The monotonically changing response and recovery times among the hybrids, as shown in Fig. 9c, reveals that the response and recovery rates are controlled by the hole-supply rate from the SWCNTs due to the different CNT contents of the hybrids.

Figure S6a shows the transient curves measured at various concentrations of methanol gas from 10 to 125 ppm at 300 °C for the 15m-4, 15m-5, 15m-6, and 15m-7 sensors. Fig. 10a summarizes the methanol-concentration-dependent response levels, which exhibit linear increases in response with methanol concentration. Since the 15m-5 sensor shows the best performance, its sensing properties were further investigated in terms of gas selectivity, repeatability, and long-term stability. The detection limit for 15m-5 sensor was determined to be 50 ppb methanol, which was derived from a linear fitting of the curve in Fig. 10a to the concentration for $R_g/R_o = 1.2$ [50]. For the gas selectivity test, the 15m-5 sensor responses to 100 ppm concentrations of $(CH_3)_2CO$, C_2H_5OH, CH_4, CO, H_2, H_2S, NH_3, NO_2, and 35 ppm methanol at 300 °C were measured, as shown in Fig. 10b, demonstrating the good selectivity for methanol among the examined gas species. The original measurements are shown in Fig. S6b. Furthermore, the repeatability over six cycles and the long-term stability over 120 days for the 15m-5 sensor to 10 ppm methanol gas at 300 °C are displayed in Fig. 10c and d, respectively. The Co_3O_4/SWCNT nanohybrid sensor exhibits good repeatability and long-term stability to methanol gas with a mean deviation of 1.9 %. All the results demonstrate the applicability of the hybrids to practical methanol sensing devices. The gas sensing

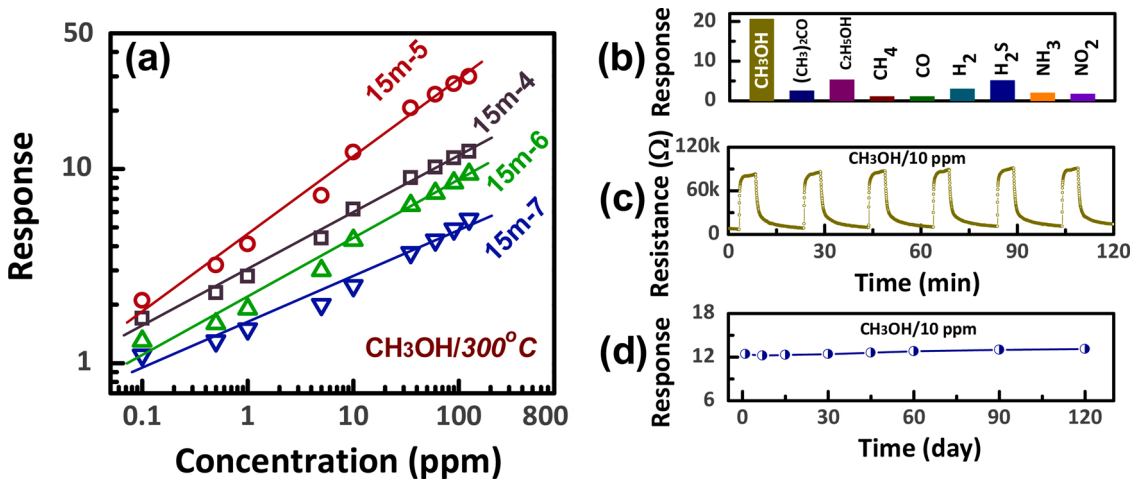

Fig. 10. (a) Response levels of 15m-4, 15m-5, 15m-6, and 15m-7 measured at 300 °C for various methanol concentrations. (b) Relative response levels of 15m-5 to 100 ppm $(CH_3)_2CO$, C_2H_5OH, CH_4, CO, H_2, H_2S, NH_3, NO_2, and 35 ppm methanol at 300 °C. (c) Repeatability for 15m-5 over six cycles and (d) long-term stability of the 15m-5 sensor to 10 ppm methanol at 300 °C measured for 120 days.

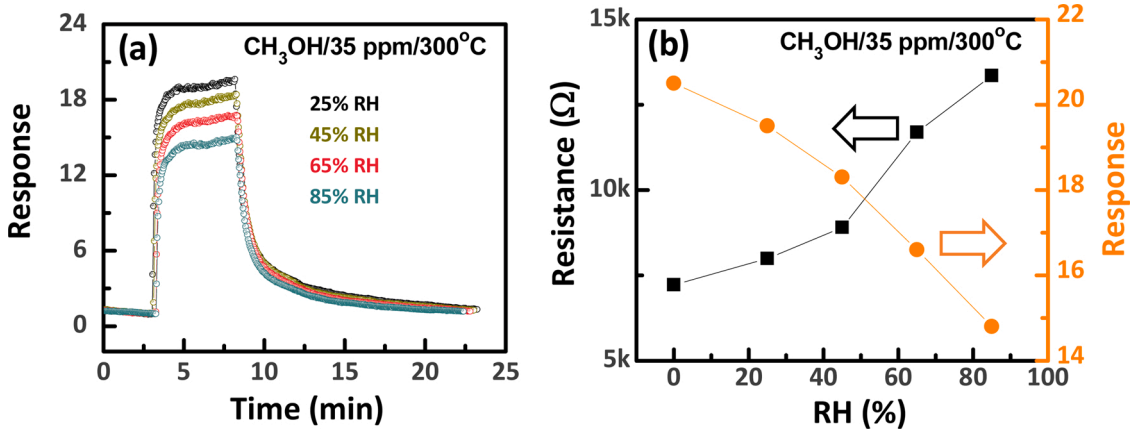

Fig. 11. (a) Transient response curves and (b) derived resistance and response of 15m-5 sensor to 35 ppm CH_3OH at 300 °C in various RH conditions (0%, 25 %, 45 %, 65 %, and 85 %).

performance of the composite structure is compared with other methanol sensors reported in the literature (Table S1). While all the different sensor structures operated at temperatures around 300 °C, our Co_3O_4/SWCNT nanohybrid structure exhibited the highest sensing response.

The exhaled breath contains a large amount of moisture, and the humidity effect on the sensing performance is important. Transient response curves of 15m-5 sensor to 35 ppm CH_3OH at 300 °C were measured in various relative humidity (RH) conditions (25%–85%), and the results are presented in Fig. 11. The baseline resistance of the sensor increased with increasing RH from ~7.2 kΩ at 0% RH to ~13.4 kΩ at 85 % RH, which led to a decrease of the response from 20.5–14.8 with the RH change. The humidity effect can be understood by the n-type doping effect of water molecules [51]. A sensing material and/or structure that is immune to humidity is preferred, but the humidity effect in our sensors was considerable at the operation temperature 300 °C and needs to be calibrated. We suggest a simple solution of using a humidity sensor in parallel at the same location [26].

4. Conclusions

Co_3O_4/SWCNT nanohybrid sensor structures were fabricated by the co-arc discharge method and show high methanol-sensing performances. While the different film thicknesses of the Co_3O_4/SWCNT nanohybrids demonstrated the effect of percolation among the highly conducting SWCNTs in the films on the film conductance and sensing properties, a finite thickness of the composite film is required for the optimum response level. A synergistic effect of the Co_3O_4/SWCNT nanohybrid was exhibited compared with the sensing performances of the pure SWCNTs and pure Co_3O_4. The optimized performance of the hybrids was exhibited by the 15m-5 sensor oxidized at 500 °C, which shows a response level of 21–35 ppm methanol at 300 °C and response and recovery times of 150 and 180 s, respectively. In addition, the origin of the enhanced sensing performance, response level, and sensing kinetics in the nanohybrid gas sensors was systematically investigated. The following observations were made:

- The SWCNTs behave as a transducer supplying holes to the Co_3O_4, which is shown to be a receptor for high-density-oxygen ionosorption.
- The hole-supplying rate from the SWCNTs determines the sensing response level and sensing kinetics for the Co_3O_4 receptor. As a result, the synergetic effect shown in the Co_3O_4/SWCNT nanohybrids is derived from the high hole-supply rate from the SWCNTs under saturated oxygen ionosorption on the Co_3O_4 surface.

In addition, the 15m-5 sensor also exhibits excellent methanol-gas-sensing properties, including low detection limit of 50 ppb, good

selectivity, repeatability, and long-term stability revealing its potential practical application for trace methanol detection in a handheld exhaled-breath test.

CRediT authorship contribution statement

Nguyen Duc Chinh: Conceptualization, Data curation, Formal analysis, Investigation, Methodology, Writing - original draft. **Nguyen Manh Hung:** Methodology. **Sutripto Majumder:** Methodology. **Chunjoong Kim:** Supervision. **Dojin Kim:** Project administration, Resources, Supervision, Writing - review & editing.

Declaration of Competing Interest

The authors report no declarations of interest.

Acknowledgments

This work was supported by the National Research Lab of the National Research Foundation of Korea (NRF-2018R1A2A1A05023126).

Appendix A. Supplementary data

Supplementary material related to this article can be found, in the online version, at doi:https://doi.org/10.1016/j.snb.2020.128956.

References

[1] B. Buszewski, M. Kęsy, T. Ligor, A. Amann, Human exhaled air analytics: biomarkers of diseases, Biomed. Chromatogr. 21 (2007) 553–566.
[2] W.B. Agnes, J.B.Nv.B. Joep, W.D. Jan, S. Agnieszka, F.W. Emile, Jv.S. Frederik, The versatile use of exhaled volatile organic compounds in human health and disease, J. Breath Res. 6 (2012), 027108.
[3] S.M. Abbott, J.B. Elder, P. Španěl, D. Smith, Quantification of acetonitrile in exhaled breath and urinary headspace using selected ion flow tube mass spectrometry, Int. J. Mass Spectrom. 228 (2003) 655–665.
[4] A.A.S. Amann, David, Breath Analysis for Clinical Diagnosis and Therapeutic Monitoring.
[5] L. Pauling, A.B. Robinson, R. Teranishi, P. Cary, Quantitative analysis of urine vapor and breath by gas-liquid partition chromatography, Proc. Natl. Acad. Sci. 68 (1971) 2374.
[6] A. Bajtarevic, C. Ager, M. Pienz, M. Klieber, K. Schwarz, M. Ligor, et al., Noninvasive detection of lung cancer by analysis of exhaled breath, BMC Cancer 9 (2009) 348.
[7] R.F. Machado, D. Laskowski, O. Deffenderfer, T. Burch, S. Zheng, P.J. Mazzone, et al., Detection of lung cancer by sensor array analyses of exhaled breath, Am. J. Respir. Crit. Care Med. 171 (2005) 1286–1291.
[8] A. France-Presse, Death Toll in Iran Alcohol Poisoning Jumps to 84, Voice of America News, 2018.
[9] S. David, More Than 100 Villagers Return Home After Methanol Poisoning, Khmer Times, 2018.
[10] K.S.H. Kumar, Over 90 Killed in India by Toxic Homemade Liquor, The New York Times, 2019.
[11] O. Laakso, M. Haapala, P. Jaakkola, R. Laaksonen, K. Luomanmaki, J. Nieminen, et al., FT-IR breath test in the diagnosis and control of treatment of methanol intoxications, J. Anal. Toxicol. 25 (2001) 26–30.
[12] N. Barsan, C. Simion, T. Heine, S. Pokhrel, U. Weimar, Modeling of sensing and transduction for p-type semiconducting metal oxide based gas sensors, J. Electroceramics 25 (2010) 11–19.
[13] H.-M. Jeong, H.-J. Kim, P. Rai, J.-W. Yoon, J.-H. Lee, Cr-doped Co3O4 nanorods as chemiresistor for ultraselective monitoring of methyl benzene, Sens. Actuators B Chem. 201 (2014) 482–489.
[14] W.Y. Li, L.N. Xu, J. Chen, Co3O4 nanomaterials in Lithium-Ion Batteries and gas sensors, Adv. Funct. Mater. 15 (2005) 851–857.
[15] X. Xie, Y. Li, Z.-Q. Liu, M. Haruta, W. Shen, Low-temperature oxidation of CO catalysed by Co3O4 nanorods, Nature 458 (2009) 746–749.
[16] I. Sayago, E. Terrado, M. Aleixandre, M.C. Horrillo, M.J. Fernández, J. Lozano, et al., Novel selective sensors based on carbon nanotube films for hydrogen detection, Sens. Actuators B Chem. 122 (2007) 75–80.
[17] Y.-P. Sun, K. Fu, Y. Lin, W. Huang, Functionalized carbon nanotubes: properties and applications, Acc. Chem. Res. 35 (2002) 1096–1104.
[18] A. Hirsch, Functionalization of single-walled carbon nanotubes, Angew. Chemie Int. Ed. 41 (2002) 1853–1859.
[19] S. Mahouche Chergui, A. Ledebt, F. Mammeri, F. Herbst, B. Carbonnier, H. Ben Romdhane, et al., Hairy carbon Nanotube@Nano-Pd heterostructures: design, characterization, and application in suzuki C−C coupling reaction, Langmuir 26 (2010) 16115–16121.
[20] N. Van Hieu, L.T.B. Thuy, N.D. Chien, Highly sensitive thin film NH3 gas sensor operating at room temperature based on SnO2/MWCNTs composite, Sens. Actuators B Chem. 129 (2008) 888–895.
[21] B.-Y. Wei, M.-C. Hsu, P.-G. Su, H.-M. Lin, R.-J. Wu, H.-J. Lai, A novel SnO2 gas sensor doped with carbon nanotubes operating at room temperature, Sens. Actuators B Chem. 101 (2004) 81–89.
[22] D. Eder, Carbon nanotube– inorganic hybrids, Chem. Rev. 110 (2010) 1348–1385.
[23] N.D. Hoa, N. Van Quy, D. Kim, Nanowire structured SnOx–SWNT composites: high performance sensor for NOx detection, Sens. Actuators B Chem. 142 (2009) 253–259.
[24] W. Li, H. Jung, N.D. Hoa, D. Kim, S.-K. Hong, H. Kim, Nanocomposite of cobalt oxide nanocrystals and single-walled carbon nanotubes for a gas sensor application, Sens. Actuators B Chem. 150 (2010) 160–166.
[25] S. Moon, N.M. Vuong, D. Lee, D. Kim, H. Lee, D. Kim, et al., Co3O4–SWCNT composites for H2S gas sensor application, Sens. Actuators B Chem. 222 (2016) 166–172.
[26] N.M. Hieu, C.V. Phuoc, T.T. Hien, N.D. Chinh, N.D. Quang, C. Kim, et al., A separated Receptor/Transducer scheme as strategy to enhance the gas sensing performance using hematite–Carbon nanotube composite, Sensors 19 (2019) 3915.
[27] D. Jung, M. Han, J. Kim, G.S. Lee, Gas-sensing properties of multi-walled carbon-nanotube sheet decorated with cobalt oxides, 14th IEEE International Conference on Nanotechnology (2014) 780–784.
[28] N.Q. Dung, D. Patil, H. Jung, D. Kim, A high-performance nonenzymatic glucose sensor made of CuO–SWCNT nanocomposites, Biosens. Bioelectron. 42 (2013) 280–286.
[29] N.D. Chinh, N.D. Quang, H. Lee, T. Thi Hien, N.M. Hieu, D. Kim, et al., NO gas sensing kinetics at room temperature under UV light irradiation of In2O3 nanostructures, Sci. Rep. 6 (2016) 35066.
[30] G.W. Thomson, The antoine equation for vapor-pressure data, Chem. Rev. 38 (1946) 1–39.
[31] S. Scaccia, M. Carewska, P.P. Prosini, Study of purification process of single-walled carbon nanotubes by thermoanalytical techniques, Thermochim. Acta 435 (2005) 209–212.
[32] H. Song, Y. Cho, M. An, Y. Kang, D. Kim, A simple approach to the fabrication of transparent single-wall carbon nanotube films of high electrical and optical performance, J. Korean Phys. Soc. 53 (2008) 2111–2114.
[33] V.G. Hadjiev, M.N. Iliev, I.V. Vergilov, The raman spectra of Co 3 O 4, J. Phys. C Solid State Phys. 21 (1988) L199.
[34] W.L. Roth, The magnetic structure of Co3O4, J. Phys. Chem. Solids 25 (1964) 1–10.
[35] S. Lefrant, I. Baltog, M. Baibarac, Surface-enhanced Raman scattering studies on chemically transformed carbon nanotube thin films, J. Raman Spectrosc. 36 (2005) 676–698.
[36] M.S. Dresselhaus, G. Dresselhaus, A. Jorio, A.G. Souza Filho, R. Saito, Raman spectroscopy on isolated single wall carbon nanotubes, Carbon 40 (2002) 2043–2061.
[37] S.A. Makhlouf, Z.H. Bakr, K.I. Aly, M. Moustafa, Structural, electrical and optical properties of Co3O4 nanoparticles, Superlattices Microstruct. 64 (2013) 107–117.
[38] T.W. Ebbesen, H.J. Lezec, H. Hiura, J.W. Bennett, H.F. Ghaemi, T. Thio, Electrical conductivity of individual carbon nanotubes, Nature 382 (1996) 54–56.
[39] C.-S. Cheng, M. Serizawa, H. Sakata, T. Hirayama, Electrical conductivity of Co3O4 films prepared by chemical vapour deposition, Mater. Chem. Phys. 53 (1998) 225–230.
[40] N.M. Vuong, D. Kim, H. Kim, Surface gas sensing kinetics of a WO3 nanowire sensor: part 1—oxidizing gases, Sens. Actuators B Chem. 220 (2015) 932–941.
[41] N.M. Vuong, D. Kim, H. Kim, Surface gas sensing kinetics of a WO3 nanowire sensor: part 2—reducing gases, Sens. Actuators B Chem. 224 (2016) 425–433.
[42] N.M. Umran, V. Bala, K. Seema, R. Kumar, Structural and electronic properties of endohedral doped SWCNTs: a DFT study, Physica E Low. Syst. Nanostruct. 65 (2015) 68–76.
[43] M. Ouyang, J.-L. Huang, C.M. Lieber, Fundamental electronic properties and applications of single-walled carbon nanotubes, Acc. Chem. Res. 35 (2002) 1018–1025.
[44] F. Buonocore, F. Trani, D. Ninno, A. Di Matteo, G. Cantele, G. Iadonisi, Ab initio calculations of electron affinity and ionization potential of carbon nanotubes, Nanotechnology 19 (2007), 025711.
[45] A. Miura, Y. Uraoka, T. Fuyuki, S. Yoshii, I. Yamashita, Floating nanodot gate memory fabrication with biomineralized nanodot as charge storage node, J. Appl. Phys. 103 (2008), 074503.
[46] X. Zhu, J. Wang, D. Nguyen, J. Thomas, R.A. Norwood, N. Peyghambarian, Linear and nonlinear optical properties of Co 3 O 4 nanoparticle-doped polyvinyl-alcohol thin films, Opt. Mater. Express 2 (2012) 103–110.
[47] J.-W. Kim, S. Lee, P. Biswas, T.I. Lee, J.-M. Myoung, Solution-processed n-ZnO Nanorod/p-Co3O4 nanoplate heterojunction light-emitting diode, Appl. Surf. Sci. 406 (2017).
[48] M. Ebadi, M. Mat-Teridi, M. Sulaiman, W. Basirun, N. Asim, N.A. Ludin, et al., Electrodeposited p-type Co 3 O 4 with high photoelectrochemical performance in aqueous medium, RSC Adv. 5 (2015) 36820–36827.
[49] E. Arciga-Duran, Y. Meas, J. Pérez-Bueno, J. Ballesteros, G. Trejo, Electrochemical synthesis of Co3O4-x films for their application as oxygen evolution reaction

electrocatalysts: role of oxygen vacancies, J. Electrochem. Soc. 165 (2018). H3178-H86.
[50] J.-S. Kim, C.W. Na, C.-H. Kwak, H.-Y. Li, J.W. Yoon, J.-H. Kim, et al., Humidity-independent gas sensors using Pr-Doped In2O3 macroporous spheres: role of cyclic Pr3+/Pr4+ redox reactions in suppression of water-poisoning effect, ACS Appl. Mater. Interfaces 11 (2019) 25322–25329.
[51] Z. Chen, C. Lu, Humidity Sensors: A Review of Materials and Mechanisms, Sens. Lett. 3 (2005) 274–295.

Nguyen Duc Chinh received his PhD in materials science and engineering at Chungnam Nat. Univ., Korea in 2019. He is now at a post doctor in Nano Materials and Application Lab. at Chungnam Nat. Univ. His current interests include nanomaterials, nanofabrication, and their applications to electronic devices: gas sensor and photoelectrochemical water splitting. **Contact:** chjnhnd@live.com

Nguyen Manh Hung received his master of materials science in Hanoi University of Science and Technology (HUST), Vietnam, in 2016. Currently, he is a PhD candidate in the Department of Materials Science and Engineering, Chungnam National University, Republic of Korea. His current research interests include nanomaterials, nanofabrication and applications to PEC water splitting and gas sensor, especially low-temperature gas sensor. Contact: manhhung.hvktqs@gmail.com

Sutripto Majumder received his Ph.D. in Department of Physics at Visvesvaraya National Institute of Technology (VNIT), Nagpur (India) in 2017. Recently, he is working as a postdoctoral fellow in Nano Materials and Application Lab. at Chungnam National University, Republic of Korea. His current research interest is synthesis and fabrication of nanostructured thin films electrodes for photoelectrochemical water splitting and solar cells. Contact: sutriptomajumdervnit2013@gmail.com

Chunjoong Kim received his Ph.D. degree in Materials Science and Engineering of Seoul National University, Korea. He is currently an associate professor in the Department of Materials Science and Engineering at Chungnam National University since 2015. His current research interests include the understanding of reaction mechanism in the materials for energy storage devices, photoelectrochemical cells, sensors. Contact: ckim0218@cnu.ac.kr

Dojin Kim received his PhD in Materials Science and Engineering at University of Southern California, USA in 1989. He is a professor of Department of Materials Science and Engineering at Chungnam Nat. Univ., Korea. His current research interests are nanostructures synthesis and applications to electronic and energy devices including gas and bio sensors, displays, transparent conducting films, electrodes for photoelectrochemical cells and solar cells. Contact dojin@cnu.ac.kr.